Computational Screening of Single Atoms Anchored on Defective Mo_2CO_2 MXene Nanosheet as Efficient Electrocatalysts for the Synthesis of Ammonia

Shuo Wang[a], Lei Li[b,*], Kwan San Hui[c,*], Feng Bin[d], Wei Zhou[e], Xi Fan[f], E. Zalnezhad[g], Jing Li[a,*], Kwun Nam Hui[a,*]

[a] Joint Key Laboratory of the Ministry of Education, Institute of Applied Physics and Materials Engineering, University of Macau, Avenida da Universidade, Taipa, Macau SAR, P.R. China. Email: bizhui@um.edu.mo

[b] Hefei National Laboratory for Physical Sciences at the Microscale, Collaborative Innovation Center of Chemistry for Energy Materials, University of Science and Technology of China, Hefei 230026, P.R. China. Email: uestclilei@163.com

[c] School of Engineering, Faculty of Science, University of East Anglia, Norwich, NR4 7TJ, United Kingdom. Email: k.hui@uea.ac.uk

[d] State Key Laboratory of High-Temperature Gas Dynamics, Institute of Mechanics, Chinese Academy of Science, Beijing 100190, P.R. China.

[e] Department of Mechanical & Electrical Engineering, Xiamen University, Xiamen 361005, P.R. China.

[f] Ningbo Institute of Materials Technology, Engineering, Chinese Academy of Sciences, Ningbo, 315201, P.R. China.

[g] Department of Chemical and Biomedical Engineering, University of Texas At San Antonio, San Antonio, TX, USA.

Abstract

Electrochemical nitrogen reduction reaction (NRR) over single-atom catalysts (SACs) anchored on Mo vacancies of Mo_2CO_2 MXene nanosheets under ambient conditions suffers from poor selectivity, low yield, and low Faradaic efficiency because of their sluggish kinetics and the competing hydrogen evolution reaction. Here, density functional theory calculations were performed to improve the understanding of the selectivity and yielding of ammonia through NRR over various isolated SACs, that is, from Sc to Au, anchored on the Mo vacancy of the Mo_2CO_2 MXene nanosheet. The potential-determining step of NRR demonstrated that eight candidates (i.e., Y, Zr, Nb, Hf, Ta, W, Re, and Os) confined on the defective Mo_2CO_2 layer could promote the electroreduction from N_2 to NH_3. The single-atom Y anchored on the defective Mo_2CO_2 (denoted as Mo_2CO_2-Y_{SA}) presented the lowest reported reaction energy barrier (0.08 eV) through the distal pathway and high selectivity to NRR compared with the previously synthesized Mo_2CO_2-Ru_{SA} with a relatively high energy barrier (0.65 eV) and poor selectivity. The results suggested that metals with low d-band center values in Mo vacancy of Mo_2CO_2 nanosheets are recommended to achieve a high NRR activity. In addition, the formation energy of Mo_2CO_2-Y_{SA} was more negative than that of the Mo_2CO_2-Ru_{SA} catalyst, suggesting that the experimental preparation of the Mo_2CO_2-Y_{SA} catalyst was highly feasible. This work lays a solid foundation for improving the rational design of MXene-based systems as efficient electrocatalysts for the synthesis

of ammonia.

Keywords: Electrocatalysis, Density functional theory (DFT) calculations, nitrogen reduction reaction, MXene, Single-single-atom catalysts (SACs)

Introduction

The reduction of nitrogen to ammonia (NH_3) plays a crucial role in modern society due to its widespread application in agriculture and industrial production.[1, 2] The Haber-Bosch (H-B) process is mainly employed in the industrial synthesis of NH_3 under high temperature and pressure. Such process is accompanied by a large consumption of fossil fuels and high CO_2 emission.[3] Thus, finding alternative efficient approaches to replace the NH_3 production by H−B is of paramount importance for energy conservation and sustainable development.[4] The electrochemical nitrogen reduction reaction (NRR) is an attractive route to produce NH_3 due to environment-friendliness under ambient conditions.[5] Metal-based materials, single-atom catalysts (SACs), metal-free materials,[6] and their compounds have been explored for NRR.[7, 8] However, the low activity (large NRR energy barrier), poor selectivity, and low Faraday efficiency of the reported catalysts severely limit their practical industrial applications.

MXene, as a promising catalytic system, have been widely investigated not only in NRR [9-14] but also in other vital electrocatalytic systems, such as hydrogen evolution reaction,[15] oxygen evolution reaction,[16] oxygen reduction reaction,[17, 18] and carbon dioxide reduction.[19-21] Given their designable structure and unique electronic properties, vacancies in MXene nanosheets provide a platform to effectively stabilize the embedded SACs.[22] This process improves the catalytic activity and

atomic utilization of the metal atoms.[23] For example, Pt-SACs supported on defective 2D $Ti_{3-x}C_2T_y$ MXene nanosheets with a Ti vacancy has been prepared via simultaneous self-reduction stabilization, offering a green route for utilizing greenhouse gas CO_2.[24] Pt-SACs anchored on the surface of Mo vacancies in double-transition metal MXene ($Mo_2TiC_2T_x$) nanosheets resulted in significantly enhanced HER catalytic activity.[23] Ru-SACs embedded on Ti_3C_2 nanosheets has led to a relatively high production yield and selectivity of NH_3 (yield: 2.3 μmol h^{-1} cm^{-2}, Faradaic efficiency: 13.13%),[25] surpassing those of other reported catalysts. In addition, Ru-SACs anchored on the surface of Mo vacancies of Mo_2CO_2 MXene nanosheets (Mo_2CO_2-Ru_{SA}) showed considerably enhanced NRR catalytic activity.[10] Nonetheless, it still remains critical for the development and discovery of other single-atom anchored MXene catalysts with higher NRR catalytic activity.

In general, MXenes terminate with the oxygen group or anion species, thus decreasing the N_2 adsorption activity and electrical conductivity.[22] Nevertheless, through a systematic rational design of MXene with specific SAC catalytic center, the insert N≡N bond may be efficiently activated and the reaction barrier may be reduced, improving the adsorption and activation of N_2 and constructing high-performance NRR catalysts. In addition, due to Mo plays an essential role in biological nitrogen fixation system, and a series of Mo-containing materials have been studied as the promising NRR catalysts.[26-30] In this work, first-principle simulation was conducted to better

understand the NRR electrocatalytic ability of 3d-, 4d-, and 5d transition metal atoms (TMs) embedded on Mo_2CO_2 MXene nanosheets with a Mo vacancy (Mo_2CO_2-V_{Mo}). The products were denoted as Mo_2CO_2-TM_{SA}. Eight candidates were first screened from more than 26 systems by setting according to the lower energy barriers of two possible potential-determining steps (PDSs) of NRR. The structure−property−performance relationship was symmetrically investigated to elucidate the reaction kinetics and mechanism of NRR. Among these candidates, only Mo_2CO_2-Y_{SA} achieved excellent NRR performance with the lowest onset potential of 0.08 V and high selectivity.

Computational details

Spin-polarized density functional theory (DFT)[31] was carried out for all calculations by using the Vienna ab initio Simulation Package (VASP).[32] The projector−augmented−wave pseudopotential[33] was used to treat the core electrons with a plane-wave cutoff energy of 450 eV, while the Perdew−Burke−Ernzerhof (PBE)[34] exchange-correlation function of the generalized gradient approximation(GGA)[35] was used to describe the electron exchange−correlation interactions. The Mo_2CO_2 supercell was set to 3 × 3 × 1 with a vacuum distance of 20 Å along the z-direction. The van der Waals interactions were considered using the DFT-D3 correction in Grimme's scheme.[36] The reciprocal space was sampled by 3 × 3 × 1 and 5 × 5 × 1 for geometry optimization and electronic structure calculations,

respectively. The maximal convergence tolerance for the force was lower than 0.02 eV/Å.[37] The projected crystal orbital Hamilton population (pCOHP) was employed to reveal the nature of the bond between the SACs and N-containing intermediates.[38] The thermodynamic stability of catalysts was evaluated by Ab initio molecular dynamics (AIMD) simulations for 5 ps at 300 K with a canonical NVT ensemble, in which the number of atoms (N), volume (V), and temperature (T) were set as constant.

Free-energy calculations

The free-energy diagram of each NRR elementary step was calculated by using the computational hydrogen electrode model proposed by Nørskov et al.[39, 40] The free energy of the electron−proton pair ($H^+ + e^-$) can be defined as half of the chemical potential of gaseous H_2 at equilibrium (0 V vs. standard hydrogen electrode). The difference of Gibbs free energy can be written as follows:

$$\Delta G = \Delta E + \Delta E_{ZPE} - T\Delta S$$

where ΔE is the difference of the reaction energies obtained by DFT calculations, ΔE_{ZPE} is the change in the zero-point energy (ZPE), T is the room temperature (T = 298.15 K), and ΔS is the change in entropy calculated by the vibrational frequency analysis. The entropies of the gas molecules (i.e., H_2, N_2, and NH_3) were taken from the NIST database.[41] The detailed calculated energies (E), zero-point energy (E_{ZPE}) *and* TS for small gas molecules (H_2, N_2, and NH_3) are summarized in **table S2**.

1
2

Results and discussion

Screening Mo_2CO_2-TM_{SA} as eNRR catalysts

The structure of Mo_2CO_2-TM_{SA} is exhibited in **Figure 1a**. Defective Mo_2CO_2 had previously been proved to be a suitable platform to stabilize transition metal Ru atoms for electrochemical NRR.[10] Inspired by the experimental findings, we designed and analyzed the NRR performance of a series of single TMs anchored on defective Mo_2CO_2. We removed one surface oxygen atom and replaced the exposed Mo by other transition metals. As shown in **Figure 1b**, we considered 26 kinds of transition metal elements of 3d, 4d, and 5d period with black tag because of the feasibility of their preparation.[23] To systematically explore and screen the NRR performance of Mo_2CO_2-TM_{SA}, we proposed four criteria based on the previous literatures,[42, 43] namely, N_2 adsorption, the first N_2 hydrogenation, the last NH_3 formation, and the formation energies of Mo_2CO_2-TM_{SA}.

According to the above criteria, we first calculated the configuration of the N_2 adsorption on each Mo_2CO_2-TM_{SA}. Given that the physical or chemical N_2 adsorption on the active sites is the first step of NRR, we tested both end-on and side-on adsorption configurations by geometry optimization. Despite the creation of a three-metal interspace as active site by the oxygen vacancy, N_2 is still difficult to adsorb on the Mo_2CO_2 surface by side-on mode. This phenomenon is due to the two negative charges repelled by the covered oxygen elements and steric effect. Hence, the initial adsorption configurations should be more favorable to end-on mode on the single-atom site. Our

calculation results further confirmed that the thermodynamically favorable interaction structure of N_2 after structural optimization indicated that all side-on configurations were transformed to end-on configurations. The distance between the metal site and the adjacent N atom ranged from 2.041 Å (for Mo) to 2.991 Å (for Os), and the adsorption energy of N_2 on the transition metal site was also calculated to be in the range from −0.10 eV (for Ru) to −0.59 eV (for Mo). This result indicated that N_2 was mainly by physical adsorption on Mo_2CO_2-TM_{SA}. The N–N bond length was also slightly elongated after adsorption compared with that of the pristine N_2. The detailed results of the bond length and adsorption energy are listed in **Table S1**. Combined with the results from N_2 adsorption and previous studies based on MXene substrate,[42] N_2 should be activated via a distal reaction pathway as shown in **Figure 1c**. Starting from the $*N_2$-adsorbed state, the N atom far from the catalytic center was attacked by three consecutive proton–electron pairs ($H^+ + e^-$) until the first NH_3 molecule was formed and released. Consequently, the remaining N atom was attacked by another three proton–electron pairs ($H^+ + e^-$). Finally, the last NH_3 molecule was released. The detailed process of the total 6-electron NRR is provided in our Supporting Information (Equations 1–10).

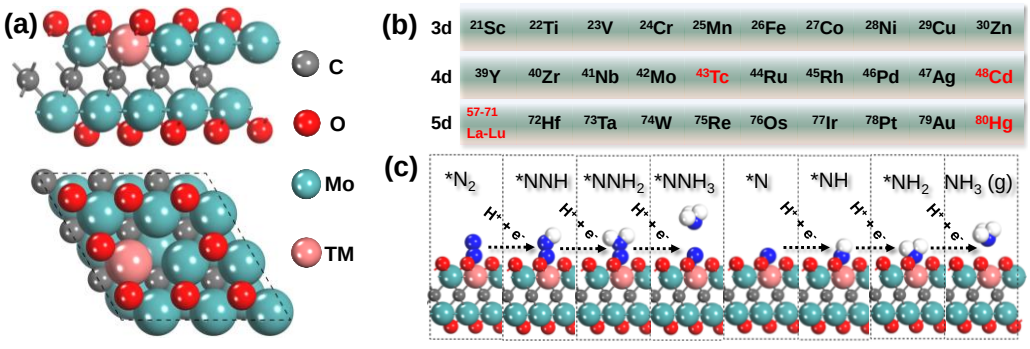

Figure 1. Atomic models and the distal pathway of nitrogen reduction. (a) Top and side views of the single-transition metal atom catalyst anchored on the Mo_2CO_2-TM_{SA} matrix. (b) A total

of 26 kinds of transition metals with black tag are considered. (c) Scheme of proton-coupled electron transfer for nitrogen reduction via a distal pathway.

Previous studies have demonstrated that the first N_2 hydrogenation ($*N_2 \rightarrow *NNH$) and the last NH_3 formation ($*NH_2 \rightarrow *NH_3$) were usually described as the potential-determining steps of the whole N_2 reduction process. With respect to the limited potential-determining step of each of the six different proton–electron elementary steps for NRR, the difference in the Gibbs energies of the N_2 hydrogenation and NH_3 formation should be minimized. Therefore, we calculated these two vital parameters on Mo_2CO_2-TM_{SA} to rapidly screen the NRR candidates. The results of $\Delta G_{(*N2 \rightarrow *NNH)}$ versus $\Delta G_{(*NH2 \rightarrow *NH3)}$ for the investigated Mo_2CO_2-TM_{SA} are plotted in **Figure 2**. Ru anchored on defective Mo_2CO_2 matrix had been successfully synthesized experimentally, and their good NRR performance was further proved.[10] Thus, the difference in the Gibbs energy of Mo_2CO_2-Ru_{SA} could be used as a benchmark for screening possible NRR materials. According to the first-principle calculation, $\Delta G_{(*N2 \rightarrow *NNH)}$ and $\Delta G_{(*NH2 \rightarrow *NH3)}$ of Mo_2CO_2-Ru_{SA} were calculated to be as high as 0.65 eV and −0.11 eV, respectively. Considering both calculations results and some typically theoretical literature,[43, 44] we finally selected 0.65 eV and 0.43 eV as the activity criteria for $\Delta G_{(*N2 \rightarrow *NNH)}$ and $\Delta G_{(*NH2 \rightarrow *NH3)}$ for the different Mo_2CO_2-TM_{SA}, respectively. The potential-determining energy of possible NRR catalysts should be close to or smaller than our defined criteria. Hence, only the Mo_2CO_2-TM_{SA} in the lower

left region, including the defective Mo_2CO_2 anchored with 3d period (Zn), 4d period (Y, Zr, and Nb), and 5d period (Hf, Ta, W, Re, Os, and Ir), were considered for the following studies. Most of the 3d metal catalytic sites, except Zn, show poor N_2 hydrogenation performance. However, numerous 4d and 5d metal sites, especially at the first half period, presented a good N_2 hydrogenation performance. The ionic radius and electrons were related to the NRR performance in our systems, which will be analysis *vide infra*.

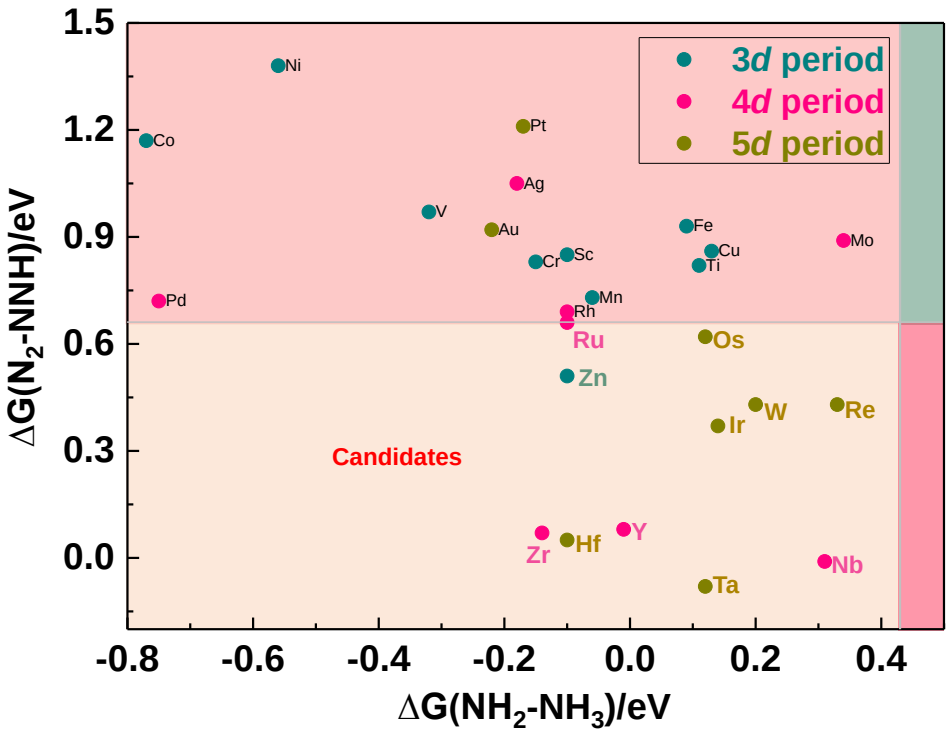

Figure 2. Screening results of Mo_2CO_2 - M_{SA} for NRR based on the changes in the free energy of the first and the last hydrogenation steps, namely, $\Delta G(N_2\text{-}NNH)$ and $\Delta G(NH_2\text{-}NH_3)$, respectively. The materials corresponding to the points in the lower left area are candidates for further investigation on the NRR processes.

Here, we further investigated the synthetic accessibility and the thermal stability of the screened candidates by computing their formation energies (E_f) and AIMD. Generally, a material with more negative value of E_f can be synthesized in the laboratory. On the contrary, materials with positive values of E_f are difficult to synthesize. Given that Mo_2CO_2-Ru_{SA} had been successfully synthesized in the experiments, the formation energy of our potential active materials should be lower than that of Mo_2CO_2-Ru_{SA}. For Zn, Y, Zr, Nb, Hf, Ta, W, Re, Os, and Ir embedded in the defective Mo_2CO_2, the formation energies were +5.48, −1.74, −3.97, −3.63, −0.49, −4.03, −4.20, −2.90, −0.52, −0.91 and +0.77 eV, respectively. Compared with the E_f criterion of Mo_2CO_2-Ru_{SA} (−0.35 eV), Mo_2CO_2-Zn_{SA} and Mo_2CO_2-Ir_{SA} should be ruled out in the candidates. Moreover, AIMD simulations were further performed to evaluate the thermodynamic stability of the remaining eight candidates, which were tested at 300 K for 5 ps with a time step of 1 fs. As shown in **Figure S1-8**, the energy and temperature of all candidates oscillated within a narrow range, and the geometric structure was basically unchanged. The results indicated that the structures of Y, Zr, Nb, Hf, Ta, W, Re and Os anchored on the defective Mo_2CO_2 can remain stable at 300 K. Hence, all candidates could be synthesized and serve as NRR electrocatalysts at ambient conditions with high stability. Finally, nearly one third of the candidates (8/26) were screened to evaluate the whole NRR process.

Reaction Mechanism and NRR Activity of Candidates

The complete reaction mechanism was investigated to evaluate the potential of the eight candidates to determine the specific hydrogenation reaction steps of the NRR catalysts. According to our above analysis and some previous studies based on defective MXene systems, an end-on N_2 adsorption model along with distal pathway was more favorable than the alternating pathway because of the special coordinated environment of the substrate of the former. The free-energy diagrams of the eight candidates are plotted in **Figures 3a–i** to elucidate the NRR mechanism in detail. In addition, the corresponding configurations for each elementary step are presented in **Figure S9-16**. To compare the theoretical simulation and experiments, the pristine Mo_2CO_2 with only one oxygen vacancy (denoted as Mo_2CO_2-Mo_{SA}) and experimentally synthesized defective Mo_2CO_2-Ru_{SA} were also considered here, and their free-energy profiles are exhibited in **Figures S17** and **S18**, respectively. For metal catalysts, the Ru(0001) surface was considered to have the highest activity and was selected as a benchmark for comparison.[45]

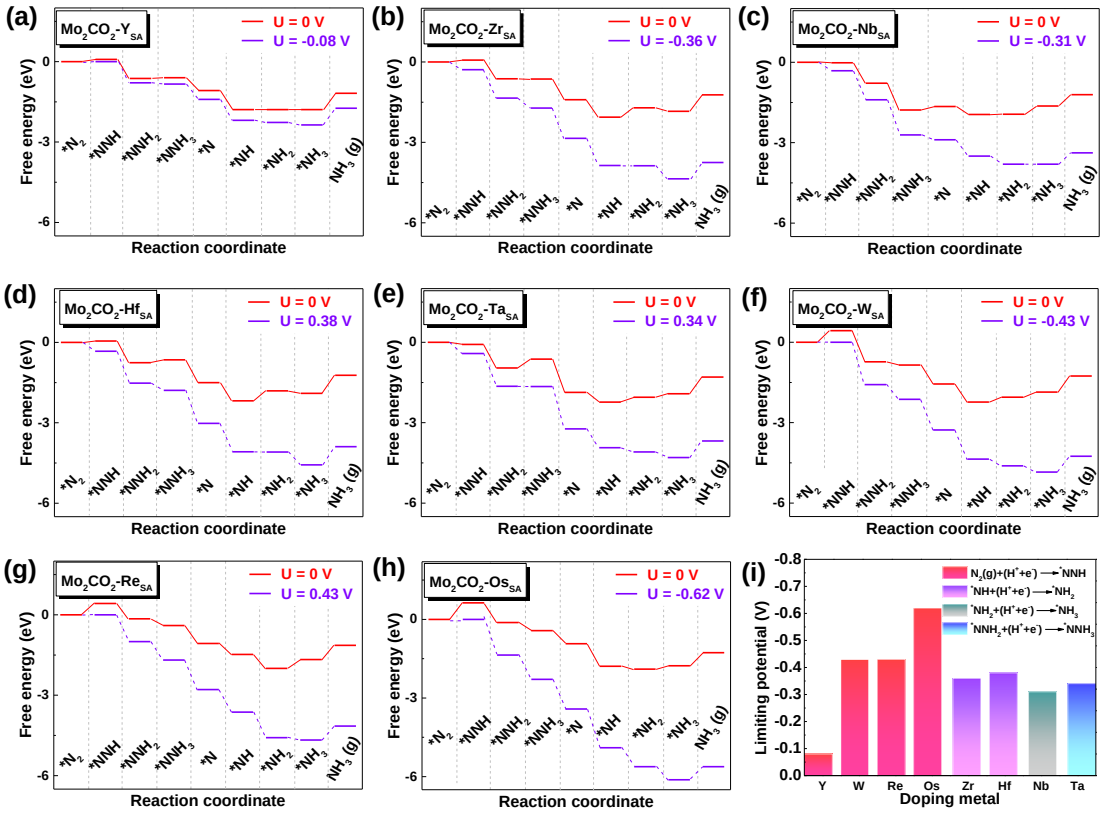

Figure 3. (a–h) Free-energy diagrams for the whole NRR process of the eight candidates at different potentials. (i) Summary of limiting potentials for eNRR via a distal pathway for transition metal single-atom catalysts on Mo_2CO_2-V_{Mo}.

The theoretical limiting potential (U_L) is often used to evaluate the intrinsic activity of catalysts. This potential is the lowest negative potential, i.e., $U_L = -\Delta G_{max}/e$, where ΔG_{max} is the maximum change in the free energy of the proton–electron step. The summarized potential determining step and related energies of the selected candidates, Mo_2CO_2-Mo_{SA} and Mo_2CO_2-Ru_{SA} are presented in **Table 1**. The limiting potential of the eight candidates surpassed that of the metal-based benchmark Ru(0001) (U_L = −1.08 V). On the basis of Y (−0.08 V), Zr (−0.36 V), and Nb (−0.31 V) for the 4d metals and Hf (−0.38 V), Ta (−0.34 V), W (−0.43 V), Re (−0.43 V) and Os (−0.62

V) for the 5d metals, eight candidates (i.e., Mo_2CO_2-Y_{SA}, Mo_2CO_2-Zr_{SA}, Mo_2CO_2-Nb_{SA}, Mo_2CO_2-Hf_{SA}, Mo_2CO_2-Ta_{SA}, Mo_2CO_2-W_{SA}, Mo_2CO_2-Re_{SA}, and Mo_2CO_2-Os_{SA}) also exhibited significantly lower limiting potential compared with Mo_2CO_2-Mo_{SA} (−0.89 eV) and experimentally prepared Mo_2CO_2-Ru_{SA} (−0.65 eV). Among the candidates, the PDS of Y, W, Re, Nb, and Os system perfectly matched our defined screening criteria, which depended on the first N_2 hydrogenation ($^*N_2 \rightarrow \cdot^*NNH$) or the last NH_3 formation ($^*NH_2 \rightarrow \cdot^*NH_3$). However, the PDSs of another three candidates were not the same as our criteria, as shown in **Figure 3i**. The PDSs of the Zr and Hf system were from $^*NNH$ to $^*NNH_2$, whereas that of the Ta system was from $^*NNH_2$ to $^*NNH_3$. Despite the differences, our screening criteria were still efficient to filter out some catalysts with higher limiting potentials. The limiting potentials of all selected candidates were not higher than our initial set value of 0.65 eV. Moreover, the potential- determining step of $^*NNH$ to $^*NNH_2$ and $^*NNH_2$ to $^*NNH_3$ have also been proved to be an essential step of the NRR process, according to previous studies.[42, 43]

Table 1. Detailed information of eight candidates, Mo_2CO_2-Mo_{SA}, and Mo_2CO_2-Ru_{SA} for comparison. Elements are arranged by atomic number. Mo_2CO_2 -Y_{SA} with the lowest ΔG_{max} is highlighted.

	$\Delta E_{N2\text{-}adsorption}$ (eV)	PDS	ΔG_{max} (eV)	$\Delta G_{NH3\text{-}desorption}$ (eV)
Y	**-0.31**	$^*N_2 \rightarrow {}^*NNH$	**0.08**	**0.61**
Zr	-0.26	$^*NH \rightarrow {}^*NH_2$	0.36	0.61

Nb	-0.28	$^{*}NH_2 \rightarrow {}^{*}NH_3$	0.31	0.42
Mo	-0.59	$^{*}N_2 \rightarrow {}^{*}NNH$	0.89	0.41
Ru	-0.07	$^{*}N_2 \rightarrow {}^{*}NNH$	0.65	0.35
Hf	-0.26	$^{*}NH \rightarrow {}^{*}NH_2$	0.38	0.67
Ta	-0.19	$^{*}NNH_2 \rightarrow {}^{*}NNH_3$	0.34	0.62
W	-0.23	$^{*}N_2 \rightarrow {}^{*}NNH$	0.43	0.59
Re	-0.35	$^{*}N_2 \rightarrow {}^{*}NNH$	0.43	0.52
Os	-0.22	$^{*}N_2 \rightarrow {}^{*}NNH$	0.62	0.50

The final NH_3 desorption process would significantly affect the yield of gas release. Previous studies have indicated that ΔG_{NH3}-desorption in the NRR was in a range of 0.4−1.3 eV.[46] This value implied that a high energy of G_{NH3}-desorption would inhibit the final NH_3 release. In our case, the NH_3 desorption processes of all candidates were endothermic in the narrow range (from 0.42 eV to 0.67 eV), and most values were lower than those of the majority of the reported SAC-supported MXene-based NRR catalysts, such as $W/Ti_{2-x}C_2O_y$ (0.95 eV),[47] $Mo_2TiC_2O_2$-Zr_{SA} (0.97 eV),[42] and Mn/Nb_2CN_2 (0.58 eV)[46]. Thus, all candidates should be recycled experimentally and have high efficiency. Then, we analyzed the Bader charge of a series of TMs to gain insight into the screening results, as displayed in **Figure S19**. The positive charge of the 3d TMs were all below 2.00 |e|, whereas the partial charge on the dopants of 4d and 5d generally decreased because the number of valence electrons increased. More importantly, the

dopants, including Y, Zr, Nb, Hf, Ta, W, and Re, showed better screening results in the first half period when the positive charge was approximately 2.00 |e|. A positively charged center can obviously polarize and activate the inert N_2 molecule.[48] Hence, doping of these SACs with larger positive charges could significantly promote the NRR process. Furthermore, the main side reaction competing with NRR in an acidic environment was HER. The limiting potential (U_L) of HER is the applied potential, that is, the step on the considered process was the most exergonic. The differences in the free energies of hydrogen adsorption were calculated on the same site of the NRR activities. The relationship[49] between $U_{L(HER)}$ and $U_{L(NRR)}$ for the eight candidate systems are shown in **Figure S20** and the related HER diagrams are presented in **Figure S21**. All candidates should have remarkably higher NRR performance than HER. Thus, all candidates are ideal electrocatalysts for NRR because of their moderate positive charge and inhibiting effect on HER.

Considering that Mo_2CO_2-Y_{SA} exhibited the lowest theoretical limiting potential among the candidates, we took Mo_2CO_2-Y_{SA} as an example to examine the whole free-energy diagram in **Figures 3a and S22**. At the beginning, N_2 was intensely physisorbed on the single Y-atom in an end-on configuration with the N−N bond length of 1.12 Å, and the distance between Y and the adjacent nitrogen was 2.61 Å. Then, the first proton coupled with an electron ($H^+ + e^-$) attacked the adsorbed $*N_2$ to produce the *NNH intermediate, with the N−N bond extended to 1.27 Å. This step activated the high

stability of the triple bond of the N_2 molecule and resulted in the maximum differences in the free energies of 0.08 eV. The subsequent changes in the free energy after the first step were almost downhill until the final NH_3 was released with a relatively low energy of 0.61 eV. The detailed calculated energies (E), zero-point energy (E_{ZPE}) *and* TS for N-containing Intermediates (*N2, *NNH, *NNH2, * NNH3, etc) are summarized in **table S3**. Unique advantages of the single-atom Y anchored on the defective MoC_2O_2 were its extremely low limiting potential (−0.08V) and moderate NH_3 desorption ability (0.61 eV), which were better than those of the majority of the reported single-atom-doped MXenes, including $W/Ti_{2-x}C_2O_y$ (−0.11 V, 0.95 eV)[47], $Ru@Mo_2CO_2$ (−0.46 V, 0.59 eV)[50], $Mo_2TiC_2O_2$-Zr_{SA} (−0.15 V, 0.97 eV)[42], and Mn-Nb_2CN_2 (−0.51 V, 0.58 eV)[46]. These characteristics indicated that Mo_2CO_2-Y_{SA} would require lower applied potential to initiate the reaction toward producing ammonia at an appropriate rate and, therefore, have better intrinsic activity.

Origin of NRR Activity on the Mo_2CO_2-M_{SAC}

Based on the free-energy diagrams, further clarification of the meaningful activity trends is very essential to provide a panorama of Mo_2CO_2-TM_{SA} for NRR. Electronic combinations of filled and empty *d* orbitals for the transition metals are well known to determine the reduction performance.[51, 52] As shown in **Figure 4**, TM atoms have empty *d* orbitals that accept lone-pair electrons from the N_2 molecule to form an σ bond, and they can also feed electrons back to the anti-bonding orbital of N_2 molecule to form

a π* bond and then weaken the inert N≡N triple bond.[51] Therefore, the charge densities differences were performed to visually prove the electronic transfer between the active site and N_2, as described in **Figures S23** and **S24**. All active sites could effectively activate N_2. The charge accumulation (yellow region) was distributed around the N≡N and N-M_{SA} bonds, while the charge depletion (cyan region) around the N≡N bonds and N-M_{SA} bonds were clearly observed. These results implied that N_2 could be activated when interacting with these TM atoms.

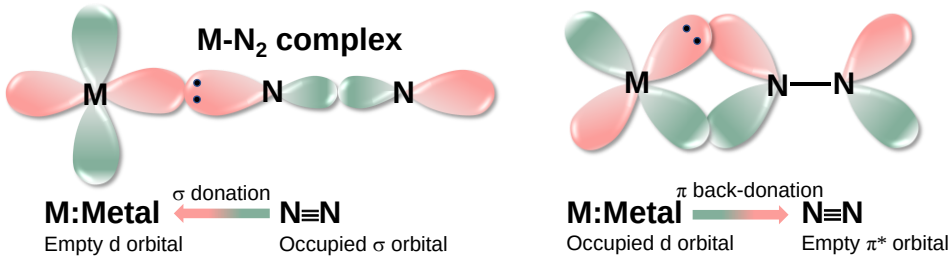

Figure 4. Simplified schematics of N_2 bonding to a transition metal atom.

Previous sections have shown that the variation in the charge at each active site determined whether the N≡N triple bond could be activated and indirectly affected the limiting potential. However, the underlying origin between the different metal centers of Mo_2CO_2-M_{SA} and ΔE_{*N2} trends remain to be explained. To reveal the underlying mechanism and the role of the different metal centers, we analyzed the various electronic structures of the screened Mo_2CO_2-TM_{SA}.

As shown in **Figure S25**, the variation in local density of state (LDOS) was plotted near the Fermi level for the adsorbed N_2 on Mo_2CO_2-TM_{SA} compared with the free N_2

molecule. The molecular orbitals of the free N_2 molecule mainly consisted of 2σ, 2σ*, 1π, 3σ, and 1π* around the Fermi level (as shown in **Figure S25 i**). This result was similar to previous theoretical results[9, 53]. After N_2 was adsorbed on the different single atoms, the peak intensity of each orbital of N_2 was weakened, and the peak shape of the orbital changed from the original slender and sharp peak to a wide and rounded one. The 1π orbital nearly disappeared, indicating that the N≡N triple bond was effectively weakened. The 1π* orbital downshifted toward the Fermi level, reflecting the accepted electrons from the M-*d* orbitals, especially for doping Y, in which the 1π* orbital downshifted at approximately 1.5 eV that is closer to the Fermi level than other cases. The electron accepting–donating interaction was directly reflected by the overlap between the N_2 orbitals and M-*d* orbital as shown in the LDOS. This result was consistent with the peak of N_2-1π* shifting away from Fermi level as the TM atomic number became larger in the same period. The increased overlapping, that is, as the TM element changed from left to right in the same period, corresponded to the decreased electron interaction between the M-*d* and N_2 and the weakened N≡N triple bond.

We further introduced the pCOHP to analyze the interaction between the metal active center and the nitrogen adatom. We followed the usual method to display COHPs, that is, bonding states were drawn to the right, and antibonding states were drawn to the left, which represented the negative and positive contributions, respectively. For Mo_2CO_2-Y_{SA} (**Figure 5a**), bonding orbital populations were detected mainly in the

valence bands (below E_F), and a small part appeared in the conduction band. Meanwhile, the antibonding states were mainly distributed in the conduction band. These phenomena explained the strong adsorption of $*N_2$ on Mo_2CO_2-Y_{SA}. However, for the doping elements Zr, Nb, Hf, Ta, W, Re, and Os, as shown in **Figure 5b−i**, the increase in the fillings of both bonding and antibonding orbital populations with the antibonding orbitals were below E_f, which was in accordance with the decreasing binding strength as indicated by the more positive ΔE_{*N2}. In addition, we calculated the integrated COHP (ICOHP) by calculating the energy integral at the E_f, which directly exhibited a slightly quantitative demonstration between ICOHP and ΔE_{*N2}, as shown in **Figure S26**. This trend indicated that the filling of the antibond orbitals below the Fermi level tended to be weak N_2 adsorption. This result validated the effect of various metal centers in determining the bonding/antibonding orbital populations on the NRR activity trends.

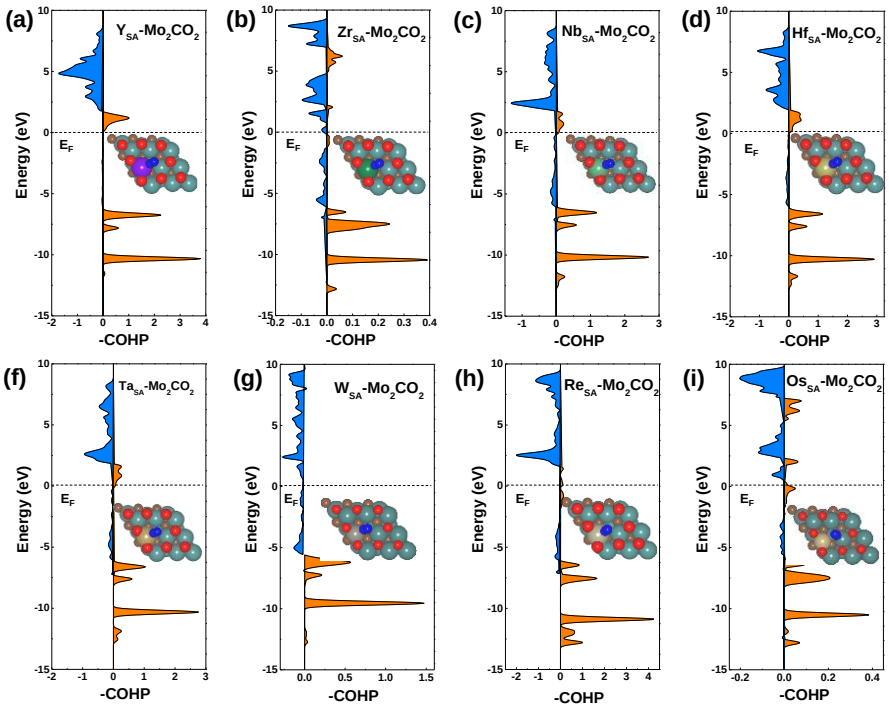

Figure 5. From (a) to (i): projected crystal orbital Hamilton population (pCOHP) between the metal center and the nitrogen adatom. Orange stands for bonding contributions, while blue stands for antibonding contributions.

Conclusions

In summary, we systematically investigated the potential of various TM-SACs anchored on the Mo vacancy of Mo_2CO_2 nanosheets on the basis of first-principle computations. By considering the first and last hydrogenation steps as the criteria, we screened eight candidates, including Y, Zr, Nb, Hf, Ta, W, Re, and Os, anchored on the defective Mo_2CO_2. All candidates could be synthesized in the laboratory due to their lower formation energy and stable dynamic performance compared with those of

Mo_2CO_2-Ru_{SA}. Mo_2CO_2-Y_{SA} had been reported as a promising candidate for NRR with a low limiting potential of −0.08 V and excellent selectivity. This work not only provided a novel type of TM-SACs supported on defective MXenes for the synthesis of ammonia but also proposed a systematic strategy for screening NRR electrocatalysts, which can be extended to other materials.

Acknowledgements

This work was funded by the Science and Technology Development Fund, Macau SAR (File no. 0191/2017/A3, 0041/2019/A1, 0046/2019/AFJ, 0021/2019/AIR), University of Macau (File no. MYRG2017-00216-FST and MYRG2018-00192-IAPME), the UEA funding. This project was partially funded by Biomechacin (Fund # BMC200101), Texas, USA. The DFT calculations were performed at High Performance Computing Cluster (HPCC) of Information and Communication Technology Office (ICTO) at University of Macau.

References

1. Chen, X.; Li, N.; Kong, Z., et al., *Mater. Horiz.* **2018,** *5* (1), 9-27.
2. Coric, I.; Mercado, B. Q.; Bill, E., et al., *Nature* **2015,** *526* (7571), 96-99.
3. Yang, X.; Nash, J.; Anibal, J., et al., *J. Am. Chem. Soc.* **2018,** *140* (41), 13387-13391.
4. Klerke, A.; Christensen, C. H.; Norskov, J. K., et al., *J. Mater. Chem.* **2008,** *18* (20), 2304-2310.
5. Montoya, J. H.; Tsai, C.; Vojvodic, A., et al., *Chemsuschem* **2015,** *8* (13), 2180-2186.
6. Li, Y.; Gao, D.; Zhao, S., et al., *Chem. Eng. J.* **2021,** *410*, 128419.
7. Yang, B.; Ding, W.; Zhang, H., et al., *Energy Environ. Sci.* **2021**.
8. Niu, H.; Wang, X.; Shao, C., et al., *ACS Sustain. Chem. Eng.* **2020,** *8* (36), 13749-13758.

9. Wang, S.; Li, B.; Li, L., et al., *Nanoscale* **2020,** *12* (2), 538-547.
10. Peng, W.; Luo, M.; Xu, X., et al., *Adv. Energ. Mater.* **2020,** *10* (25).
11. Guo, X.; Gu, J.; Lin, S., et al., *J. Amer. Chem. Soc.* **2020,** *142* (12), 5709-5721.
12. Xu, X.; Sun, B.; Liang, Z., et al., *ACS Appl. Mater. Inter.* **2020,** *12* (23), 26060-26067.
13. Sun, J.; Kong, W.; Jin, Z., et al., *Chinese Chemical Letters* **2020,** *31* (4), 953-960.
14. Luo, Y.; Chen, G.-F.; Ding, L., et al., *Joule* **2019,** *3* (1), 279-289.
15. Wang, X.; Wang, C.; Ci, S., et al., *J. Mater. Chem. A* **2020,** *8* (44), 23488-23497.
16. Ma, T. Y.; Cao, J. L.; Jaroniec, M., et al., *Angew. Chem. Int. Ed.* **2016,** *55* (3), 1138-1142.
17. Liu, C.-Y.; Li, E. Y., *Acs Applied Materials & Interfaces* **2019,** *11* (1), 1638-1644.
18. Lin, H.; Chen, L.; Lu, X., et al., *Science China-Materials* **2019,** *62* (5), 662-670.
19. Yan, Y.; Chen, J.; Li, N., et al., *Acs Nano* **2018,** *12* (4), 3523-3532.
20. Xiao, Y.; Zhang, W., *Nanoscale* **2020,** *12* (14), 7660-7673.
21. Li, L.; Li, B.; Guo, H., et al., *Nanoscale* **2020,** *12* (29), 15880-15887.
22. Liu, A.; Liang, X.; Ren, X., et al., **2020,** *30* (38), 2003437.
23. Zhang, J.; Zhao, Y.; Guo, X., et al., *Nature Catalysis* **2018,** *1* (12), 985-992.
24. Zhang, X.; Lei, J.; Wu, D., et al., *J. Mater. Chem. A* **2016,** *4* (13), 4871-4876.
25. Liu, A.; Gao, M.; Ren, X., et al., *Nanoscale* **2020,** *12* (20), 10933-10938.
26. Burgess, B. K.; Lowe, D. J., *Chem. Rev.* **1996,** *96* (7), 2983-3012.
27. Stüeken, E. E.; Buick, R.; Guy, B. M., et al., *Nature* **2015,** *520* (7549), 666-9.
28. Zhao, J.; Chen, Z., *J Am Chem Soc* **2017,** *139* (36), 12480-12487.
29. Jasin Arachchige, L.; Xu, Y.; Dai, Z., et al., *J. Phys. Chem. C* **2020,** *124* (28), 15295-15301.
30. Li, L.; Li, B.; Guo, Q., et al., *J. Phys. Chem. C* **2019,** *123* (23), 14501-14507.
31. Grimme, S., *J. Comput. Chem. Mater.* **2006,** *27* (15), 1787-1799.
32. Kresse, G.; Furthmuller, J., *Phys. Rev. B* **1996,** *54* (16), 11169-11186.
33. Blochl, P. E., *Phys. Rev. B* **1994,** *50*, 27-30.
34. Perdew, J. P.; Wang, Y., *Phys. Rev. B: Condens. Matter.* **1992,** *46* (20), 12947-12954.
35. Perdew, J. P.; Burke, K.; Ernzerhof, M., *Phys. Rev. Lett.* **1996,** *77* (18), 3865-3868.
36. Grimme, S.; Antony, J.; Ehrlich, S., et al., *J. Chem. Phys.* **2010,** *132* (154104), 1-19.
37. J, H.; Monkhorst; D.Pack, J., *Phys. Rev. B* **1976,** *13*, 5188-5192.
38. Maintz, S.; Deringer, V. L.; Tchougreeff, A. L., et al., *J. Comput. Chem.* **2016,** *37* (11), 1030-5.
39. Peterson, A. A.; Abild-Pedersen, F.; Studt, F., et al., *Energy Environ. Sci.* **2010,**

3 (9), 1311-1315.
40. Rossmeisl, J.; Logadottir, A.; Nørskov, J. K., *Chem. Phys.* **2005,** *319* (1-3), 178-184.
41. Carper, J., *Library Journal* **1999,** *124* (10), 192-+.
42. Li, L.; Wang, X.; Guo, H., et al., *Small Methods* **2019,** *1900337*, 1-7.
43. Ling, C.; Ouyang, Y.; Li, Q., et al., *Small Methods* **2019,** *3* (9).
44. He, T.; Puente Santiago, A. R.; Du, A., *J. Catal.* **2020,** *388*, 77-83.
45.Skulason, E.; Bligaard, T.; Gudmundsdottir, S., et al., *Phys. Chem. Chem. Phys.* **2012,** *14* (3), 1235-1245.
46. Kong, Y.; Liu, D.; Ai, H., et al., *ACS Appl. Nano Mater.* **2020,** *3* (11), 11274-11281.
47. Tang, S.; Liu, T.; Dang, Q., et al., *J. Phys. Chem. Lett.* **2020,** *11* (13), 5051-5058.
48. Choi, C.; Back, S.; Kim, N.-Y., et al., *ACS Catalysis* **2018,** *8* (8), 7517-7525.
49. Li, Y.; Gao, D.; Zhao, S., et al., *Chem. Eng. J.* **2021,** *410*.
50. Huang, B.; Li, N.; Ong, W.-J., et al., *J. Mater. Chem. A* **2019,** *7* (48), 27620-27631.
51. Legare, M.-A.; Belanger-Chabot, G.; Dewhurst, R. D., et al., *Science* **2018,** *359* (6378), 896-899.
52.Ling, C.; Niu, X.; Li, Q., et al., *J. Am. Chem. Soc.* **2018,** *140* (43), 14161-14168.
53. Zhu, H.-R.; Hu, Y.-L.; Wei, S.-H., et al., *.J Phys. Chem. C* **2019,** *123* (7), 4274-4281.